Journal of Ultrafine Grained and Nanostructured Materials
https://jufgnsm.ut.ac.ir
Vol. 59, No.1, June 2026, pp. 49-64
Print ISSN: 2423-6845 Online ISSN: 2423-6837
DOI: 10.22059/jufgnsm.2026.01.05

Ambient Blade-Coating of Perovskite Absorber Layer: Optimizing Process Parameters and Surfactant Concentration

Hanieh Sharifian [a,b], Maryam Heidariramsheh [c]*, Mozhdeh Forouzandeh [d], Amirali Masoudi [a]*, Nima Taghavinia [b,e]

[a] Department of Condensed Matter Physics, Faculty of Physics, Alzahra University, Tehran, Iran
[b] Nanoparticles and Coatings Lab, Department of Physics, Sharif University of Technology, Tehran, Iran
[c] School of Metallurgy and Materials Engineering, College of Engineering, University of Tehran, Tehran, Iran
[d] Solaires Enterprises Inc, Victoria, BC, V9B 4G2, Canada
[e] Center for Nanoscience and Nanotechnology, Sharif University of Technology, Tehran, Iran

Recieved: 8 May 2026; Accepted: 20 June 2026

*Corresponding author, E-mail: m.heidariramsheh@ut.ac.ir, masoudi@alzahra.ac.ir

ABSTRACT

Blade coating is a scalable deposition technique suitable for the large-area fabrication of perovskite solar cells (PSCs), offering a promising alternative to conventional spin coating. In this study, bladecoating parameters for depositing mixed triplecation–anion perovskite absorber layers were systematically optimized in planar PSCs with the structure Glass/ In-doped tin oxide (ITO) /SnO_2/perovskite/$CuInS_2$/carbon. Key processing parameters—including blade–substrate gap, coating speed, ink injection volume, and precursor concentration—were investigated to obtain uniform and highquality perovskite films. Optimal conditions were achieved at a blade–substrate gap of 0.1 mm, a coating speed of 200 mm min^{-1}, and a 1.5 M precursor solution delivered with 2 µL of ink, yielding compact and uniform films. The effect of the nonionic surfactant Triton X100 (TX100) was further explored to enhance ink wettability and film formation. Low concentrations of TX100 improved surface coverage and produced denser films, while higher concentrations resulted in smaller grain sizes, increased surface roughness, and reduced film thickness. Optical characterization showed an increase in film transmittance with increasing TX100 concentration, and photoluminescence measurements indicated enhanced emission at moderate concentrations due to defect passivation at grain boundaries. Photovoltaic measurements revealed that devices fabricated with 2 mM TX100 delivered the best performance, achieving a champion power conversion efficiency (PCE) of 14.76% and an average PCE of 13.83%. At higher TX100 concentrations, device performance degraded significantly due to poor morphology and reduced charge transport.

Keywords: *Perovskite solar cells (PSCs), Meniscusguided Blade coating, Ambient processing, Surfactant.*

1. Introduction

Perovskite solar cells (PSCs) have reached a certified power conversion efficiency (PCE) of about 27.0%, while crystalline silicon solar cells have achieved efficiencies of around 28 % [1-3]. Since the development of solid-state PSCs in 2012, their performance has improved rapidly. PSCs are especially attractive because they can be fabricated through solution-based, low-temperature processes. This offers the potential for lower production cost and reduced energy consumption compared with conventional photovoltaics. Such advantages make PSCs promising candidates for terawatt-scale electricity generation. However, scalable manufacturing of perovskite solar modules remains a major challenge. A clear efficiency gap still exists between small-area cells and large-area modules. This gap mainly arises from difficulties in controlling perovskite film formation during large-scale coating processes [2-4].

Hybrid perovskites exhibit exceptional optoelectronic properties, including high chargecarrier mobility arising from their favorable electronic band structure and strong light absorption due to their direct bandgap [5]. Mixedhalide compositions display significantly enhanced carrier diffusion lengths compared with singlehalide perovskites, with $MAPbI_3$ showing diffusion lengths around ~100 nm while $MAPbI_{3-x}Cl_x$ can exceed 1 μm. Singlecrystal $MAPbI_3$ also demonstrates extremely low trap densities (~10^9–10^{10} cm^{-3}), comparable to highquality crystalline silicon. These characteristics enable carrier diffusion lengths greater than 10 μm, allowing efficient collection of photogenerated charges and minimizing recombination losses, thereby improving photovoltaic performance in perovskite solar cells [6-8].

To achieve high PCE for perovskite solar cells, one of the most crucial prerequisites is the preparation of a high-quality perovskite layer. The morphology of hybrid perovskites strongly depends on the crystallization process, which is highly influenced by various factors including chemical composition, deposition techniques, the effect of solvents and additives during the process. To achieve high performance in perovskite solar cells, perovskite thin films with high surface coverage, a smooth surface, and larger crystalline domains are desirable [9-11].

To date, various deposition methods have been reported for fabricating high-quality perovskite layers for photovoltaic applications. These methods are generally categorized into evaporation-based deposition methods and solution-based deposition methods [12]. Although evaporation-based deposition can form relatively large and uniform layers, it is not compatible with large-scale production due to complex vacuum equipment and long processing times. Given these limitations, most research focuses on solution-based strategies for the commercialization of perovskite solar cells. Solution-based methods are low-cost strategies that can be processed at low temperatures under ambient conditions. Spin-coating is the most widely used solution-based method. Based on conducted research, almost all high-efficiency perovskite solar cells are fabricated using this method. However, spin-coating has a very low throughput and wastes a large amount of precursor solutions, making it unsuitable for large-scale production. In contrast, other solution-based deposition methods such as blade printing, slot-die printing, inkjet printing, etc., are suitable options for fabricating large-area perovskite solar cells. The meniscus-based printing method refers to a large-scale fabrication process involving the formation of a meniscus-shaped liquid edge from the desired solution to spread over a substrate surface. Under surface tension force and shear force generated by the coating head, it forms a meniscus liquid shape. Common methods of meniscus-based printing include dip coating, blade coating, and slot-die coating. Blade coating and slot-die coating are the most promising and repeatable strategies for depositing perovskite layers on a large scale. They also have rolltoroll (R2R) production capability, which has great potential for mass production of large, high-efficiency solar panels [13,14]. In this study, the doctor blade method was used. Blade coating is one of the most widely used methods for spreading solutions onto a substrate. It is also known as "doctor blade" or "knife coating". The solution is initially applied in the gap between the blade head and the substrate. In the next step, the blade moves across the substrate, creating a uniform layer of the solution. The thickness of the layer also depends on the distance of the blade from the substrate and the blade speed. Overall, meniscus-based printing methods appear to be the most promising and practical technology for fabricating large-area PSCs due to their significant advantages. First, meniscus-based printing methods are comprehensive technology compatible with various inks of different viscosities. Second, the thickness of the dried printed layer can be easily and accurately controlled within a few nanometers or up to tens of micrometers by adjusting printing parameters, such as ink injection volume, solution concentration, solution viscosity, printing speed, distance between the head and the substrate, meniscus length, and substrate temperature during deposition. Third, the meniscus-based printing process has very low ink waste compared to other deposition methods like spin coating or spray coating, which is beneficial for saving costs in large-scale industrial PSC production. The last and most important advantage is that meniscus-based printing methods are compatible with R2R manufacturing, which not only has the potential for flexible cell fabrication but also enables high-speed production [15].

The transition from lab-scale spin coating to scalable blade coating necessitates precise control over the ink's fluid dynamics and drying kinetics to ensure film uniformity. Surfactants have emerged as critical additives to modulate the surface tension of perovskite precursor inks, facilitating superior wetting on typically hydrophobic charge transport layers, such as PTAA. Beyond improving substrate coverage, surfactants like L-α-Phosphatidylcholine (LP) and CTAB suppress Marangoni instabilities and convective flows during the drying process, which prevents the formation of pinholes and ensures a smooth, mirror-like morphology across large areas. Furthermore, certain surfactants act

as chemical passivators; their functional groups can coordinate with uncoordinated ions at grain boundaries, effectively reducing trap density and enhancing charge carrier lifetimes [16-18].

In this research, we used a planar structure with a tin dioxide (SnO_2) electron-transporting layer (ETL), which is a low-temperature processable and aligns with the goals of large-scale PSC printing. To reduce material costs, improve cell stability, simplify the cell fabrication process, and consequently enable large-scale deposition of PSCs, carbon paste was employed as the back electrode in this research. Additionally, the copper indium sulfide (CIS) ink was used as the hole-transporting layer (HTL) to reduce the raw material costs for PSC fabrication. The blade-coating method is the most common printing technique for perovskite layers, alongside spin-coating in laboratory scale, due to its high efficiency and layer thickness controllability. Most importantly, blade-coating is a meniscus-based printing technique, and the results developed from this method can be easily transferred to slot-die coating for large-scale production [19]. A vacuum pump was used for rapid solvent removal and formation of intermediate phase.

2. Experimental

2.1. Materials and Methods

N,N-dimethyl formamide (DMF, 99.8%), dimethyl sulfoxide (DMSO, 99.9%), chlorobenzene (99.9%), ethanol (99.99%), and acetonitrile (99.9%) all were provided by the Merck Co. CsI (99%), was supplied by Sigma Aldrich Co. In addition, lead (II) iodide (PbI_2, IRASOL Co.), lead (II) bromide ($PbBr_2$, IRASOL co), formamidine iodide (FAI, Great cell solar), and methylammonium bromide (MABr, Great cell solar) were used. All the chemicals and solvents were kept in the glovebox before starting our experiment. $CuInS_2$ nanoparticle dispersion ink in chloroform and carbon paste was purchased from IRASOL. SnO_2 colloidal dispersion (15 % in H_2O) was purchased from Alfa Aesar. Triton-x100 was purchased by the Sigma Aldrich Co.

The solar cell designed in this study possesses a planar architecture with the layer sequence of Glass/ In-doped tin oxide (ITO)/ETL/PSK/HTL/Carbon, as illustrated in Figure 1a. In this configuration, the ETL is deposited using SnO_2 colloidal dispersion, the lightabsorbing perovskite layer consists of

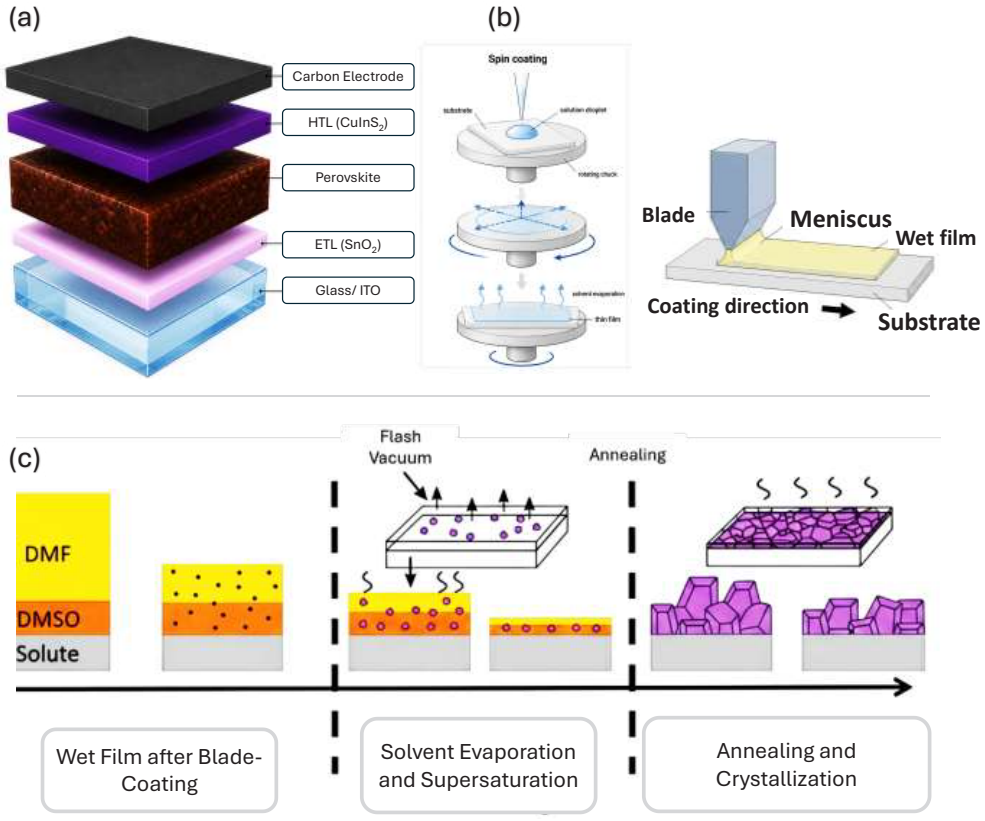

Fig. 1- (a) Schematic representation of the fabricated perovskite solar cell structure. (b) The two deposition methods—spin coating and meniscus-based blade coating—are compared as the primary techniques for film formation. (c) The transformation of the perovskite layer is depicted.

a mixed triplecation–anion composition, the HTL employs CIS ink, and the back electrode is deposited using carbon paste. To fabricate solar cells, initially a desired pattern region of the ITO substrate (dimension 7 × 2.8 cm^2) is chemically etched by masking the desired area with Scotch tape. Using zinc powder and hydrochloric acid solution, the unmasked ITO region—approximately 5 mm wide—is selectively removed. Subsequently, the substrate is cut into pieces of 1.4 × 1.4 cm^2 and 1.4 × 2.8 cm^2. The substrate cleaning process begins with rinsing the samples using a diluted detergent solution followed by deionized water. The procedure continues with sequential sonication in ethanol and isopropanol for 15 minutes each, ensuring complete surface cleanliness. For ETL deposition, SnO_2 colloidal dispersion is diluted with deionized water in a 1:5 weight ratio. The resulting solution is filtered through a 220 nm filter to remove large particles. Before spincoating, the substrates are exposed to UVOzone treatment for 30 min to enhance wettability and eliminate surface organics. The SnO_2 layer is then deposited by spincoating at a speed of 4000 rpm for 30 s, using 50 μL of solution per 1.4 × 1.4 cm^2 substrate. The coated layer, approximately 20 nm thick, is annealed at 150 °C for 30 min.

Figure 1b illustrates the comparative fabrication pathways in this study. The two deposition methods—spin coating and meniscus-based blade coating—are compared as the primary techniques for film formation. In Figure 1c the transformation of the perovskite layer is depicted, where both methods undergo a vacuum-flash treatment to trigger supersaturation followed by hotplate annealing for final crystallization. Although both techniques share these post-deposition steps, the initial wet films produced by spin coating and blade coating differ in thickness and residual solvent volume (DMF/DMSO). This variation necessitates different solvent evaporation kinetics during the vacuum process, which ultimately influences the nucleation, grain growth, and final microstructure of the perovskite thin films.

The absorber layer consists of the mixed triplecation–anion perovskite composition $Cs_x(FA_{0.83}MA_{0.17})_{1-x}Pb(I_{0.83}Br_{0.17})_3$. Although singlecation perovskites such as $MAPbI_3$ and $FAPbI_3$ are commonly used in largearea devices, the mixedcation system provides superior optical properties and enhanced stability. To prepare the perovskite precursor solution inside a glovebox, powders of PbI_2 (548.6 mg), $PbBr_2$ (57.06 mg), FAI (178.94 mg), MABr (17.41 mg), and CsI (27.02 mg) are weighed and mixed. Subsequently, DMF (780 μL) and DMSO (220 μL) solvents are added. The mixture is stirred at 70 °C until a clear yellow solution forms. As spincoating is a widely used deposition technique for laboratoryscale perovskite solar cells, it was employed here to fabricate a 1.4 × 1.4 cm^2 reference cell for comparison with the printed samples. Before spincoating the perovskite film, the substrates undergo another 30min UVOzone treatment. During deposition, the perovskite precursor is dispensed over the substrate surface using a micropipette, ensuring complete coverage. The spincoating procedure consists of 1000 rpm for 10 s followed by 6000 rpm for 30 s. In the final 20 s, 270 μL of chlorobenzene is injected as an antisolvent to improve film morphology. The films are then annealed at 100 °C for 1 hour. All perovskite deposition steps are conducted inside a dry glovebox. The blade coating was also performed using a QUANTUM 2020 3D printer. Employing a 3D printer enables precise control of coating parameters—such as blade speed and gap—through programmable commands, thus ensuring reproducible and comparable results over time. A vacuum chamber was employed to extract residual solvent from the freshly deposited perovskite layer, serving as a replacement for the conventional antisolvent process. Notably, all printing steps were performed under ambient air conditions at 40% relative humidity, unlike the reference samples, which were fabricated in dry air at low humidity levels. The printer's standard head was replaced by a metal blade for coating. Kapton tape was used between the blade and ink to improve wettability and meniscus formation; the tape was replaced after each coating cycle. Details of the bladecoating parameters are presented in Table 1. To investigate the effect of Triton X-100 (TX-100), the precursor ink of a mixed-cation and mixed-anion perovskite, was first prepared according to above-mentioned

Table 1- Blade-coating parameters for the perovskite layer

Category	Variable	Value/Condition
PSK precursor parameters	formulation	$Cs_{0.05}[(MA_{0.17}FA_{0.83})Pb(Br_{0.17}I_{0.83})_3]_{0.95}$
	Ink concentration	1 M, 1.5 M
Printing parameters	Blade–substrate gap	0.1 mm, 0.2 mm, 0.3 mm
	Coating speed	50, 100, 150 mm min^{-1}
	Ink injection volume	2 μL and 3 μL per 2.8 × 1.4 cm^2 substrate
	Post-deposition Process	Vacuum (< 100 Pa) for 30 s, thermal annealing at 100 °C for 30 min
Environmental conditions		Ambient humidity, 40–50 %
		Ambient temperature, 25–30 °C

procedure. Then, by adding a diluted solution of TX-100 (in DMSO: DMF solvent with a ratio of 1:4) into the perovskite precursor ink at different concentrations (2-12 mM), the role of TX-100 as a surfactant on the quality and photovoltaic performance of the blade-coated perovskite layers was examined.

For the HTL deposition, a CIS ink was used, containing 10–15 nm nanoparticles at a concentration of 25 mg/mL in chloroform. After cooling the perovskite layer, CIS deposition was immediately performed using 60 µL of solution per 1.4 × 1.4 cm^2 substrate at 3000 rpm for 10 s. The films were dried at 100 °C for 10 minutes. To achieve an optimal thickness of approximately 120 nm, the coating step was repeated twice. For larger substrates (1.4 × 2.8 cm^2), 120 µL of CIS ink was used. Finally, the carbon back electrode was deposited using doctorblade coating of carbon paste. After removing the masking tapes, the samples were heated at 100 °C for 30 min to dry the carbon layer. The final carbon electrode thickness was approximately 60 µm.

2.2. Characterization

Field emission scanning electron microscope (FESEM, TESCAN, Mira 3-XMU) was used for the microscopic view of the PSK films. Transmittance spectra were evaluated by a Perkin Elmer Lambda 25 UV/VIS spectrophotometer. Photoluminescence (PL) spectroscopy was carried out using Avantes-DH-S-BAL. Incident photon-to-current efficiency (IPCE) was taken in a wavelength range from 350 to 800 nm by IRASOL IPCE-015 equipment. Photovoltaic parameters were investigated using a solar simulator (IRASOL, SIM-1000) at 100 mW.cm^{-2} illumination AM 1.5 G, calibrated with a standard silicon solar cell. Since the quality assessment of the blade-coated perovskite layer relies on its comparison with the spin-coated reference layers, planar PSCs were simultaneously fabricated via spin coating to serve as control samples.

The equation 1 is a Beer–Lambert absorption equation used to determine the thickness of a film from its optical transmittance at 555 nm [20]. The absorption coefficient α is constant for the same material at the same wavelength (555 nm). So, measurements from two same material samples give:

$$\alpha = \frac{-\ln(T_1)_{\lambda=555\,nm}}{d_1} = \frac{-\ln(T_2)_{\lambda=555\,nm}}{d_2} \quad (1)$$

where α is the absorption coefficient of the material, T is the transmittance of the sample, d is the thickness of the sample. The optical and PL measurements was performed on Glass/SnO_2 substrates, while film morphology and photovoltaic measurements were conducted on ITO/SnO_2 device structures.

3. Results and Discussion

To optimize the blade-coating process, several parameters including the head speed, blade–substrate gap, perovskite solution injection volume, and solution concentration were systematically varied to examine their influence on film quality. To evaluate the quality of the bladecoated perovskite films, Uv-Vis spectroscopy was performed and compared with an optimized spincoated reference film. The absorption spectra were analyzed to examine lightharvesting capability, possible scattering effects related to film morphology, and to estimate the optical band gap of the perovskite layer. The coating speeds were set to 50, 100, and 150 mm min^{-1}, gaps to 0.1, 0.2, and 0.3 mm, injection volumes to 2 µL and 3 µL, and precursor concentrations to 1 M and 1.5 M. Other process conditions were maintained constant as listed in Table 1 throughout the blade-coating procedure. Figure 2 presents photos of blade-coated perovskite films deposited on Glass/SnO_2 substrates. The films were produced using 1 M perovskite precursor ink at coating speeds of 50, 100, and 150 mm min^{-1} and blade–substrate gaps of 0.1, 0.2, and 0.3 mm. Visual inspection of the images indicates that the perovskite layer deposited at a coating speed of 150 mm min^{-1} and a blade–substrate gap of 0.1 mm exhibits a uniform surface coverage, indicating improved film homogeneity compared with the other samples. During the printing process, it was observed that at larger blade–substrate gaps (0.2 mm and 0.3 mm), the meniscus length tended to diminish as the blade advanced, leading to incomplete deposition and consequently poor-quality perovskite layers. Based on experimental observations and the corresponding absorption–transmission spectra, the optimal gap was determined to be 0.1 mm.

As shown in Figure 3a and Figure 3b, the bladecoated film prepared with this gap exhibits an absorption trend similar to that of the spincoated reference layer. With the blade–substrate gap fixed at 0.1 mm, the absorption and transmission spectra of perovskite films printed at blade-coating speeds of 50, 100, and 150 mm min^{-1} were compared with those of the spin-coated reference perovskite layer, as shown in Figure 3c, d increasing the coating speed up to 150 mm min^{-1} resulted in an increase in optical absorption and a decrease in transmittance within the visible-light region. Additionally, the images in Figure 2 show that the sample prepared at 150 mm min^{-1} with a 0.1 mm gap displays a noticeably darker color, indicative of enhanced film thickness and coverage. When the blade-coating speed exceeds the solvent evaporation rate of the meniscus—such that a wet film remains on the substrate after coating—the deposition operates under the Landau–Levich regime [19]. In this regime, the film thickness scales directly with coating speed, meaning that faster blade

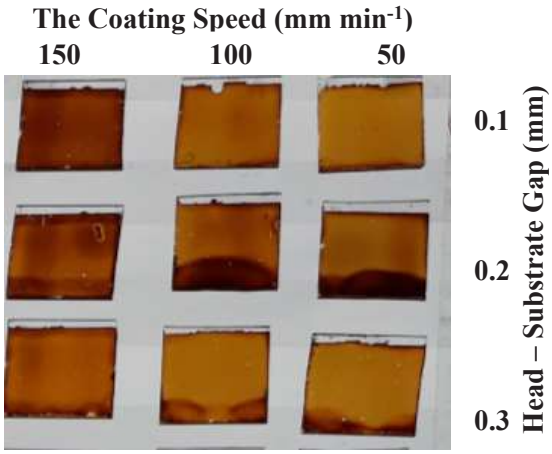

Fig. 2- Visual comparison of blade coated perovskite films produced at different coating speeds (50, 100, and 150 mm min^{-1}) and head–substrate gaps (0.1, 0.2, and 0.3 mm).

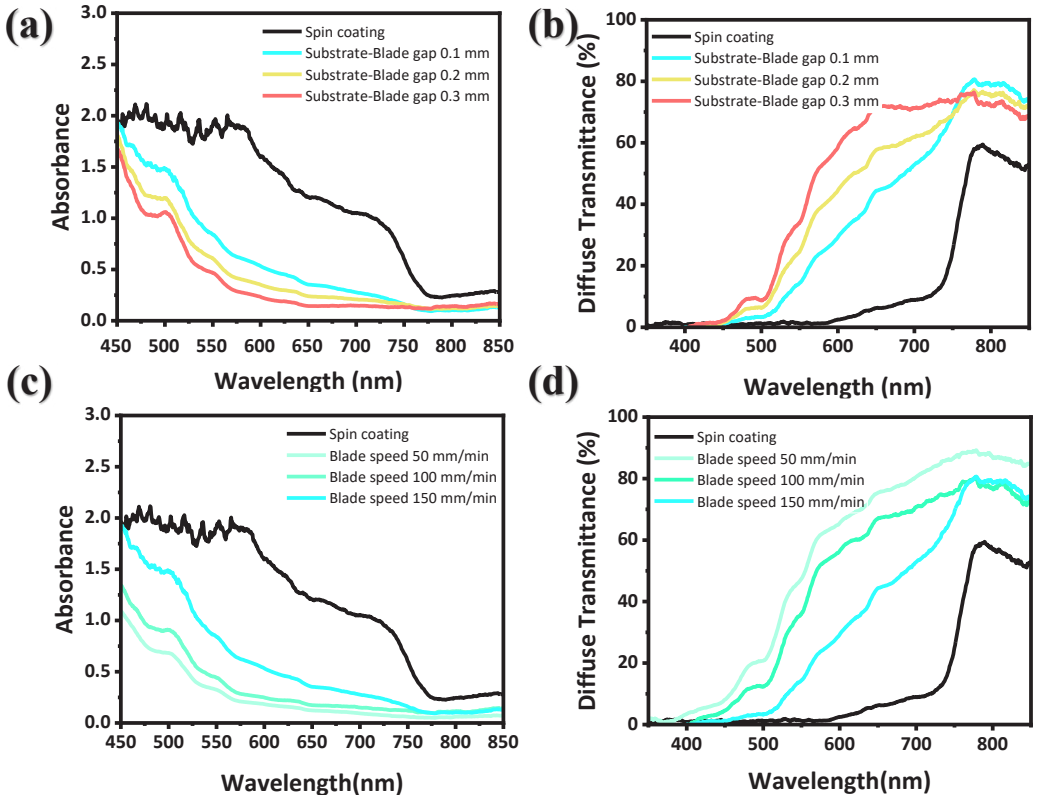

Fig. 3- (a) Absorption spectra and (b) transmittance spectra of blade-coated perovskite films at blade–substrate gaps of 0.1 mm, 0.2 mm, and 0.3 mm, recorded at a blade-coating speed of 150 mm min^{-1}. (c) Absorption spectra and (d) transmittance spectra of blade coated perovskite films at blade coating speeds of 50, 100, and 150 mm min^{-1} with a blade–substrate gap of 0.1 mm.

motion yields thicker perovskite layers. In this study, since a wet layer was consistently observed after the coating process, the fabrication is inferred to follow the Landau–Levich behavior. Consequently, both the spectroscopy results and appearance of layers confirm that increasing the blade-coating speed leads to higher film thickness for the blade-printed perovskite layers. Based on the absorption and transmission results presented in Figure 3, the perovskite layer fabricated using the bladecoating method at 150 mm min^{-1} with a 0.1 mm blade–substrate gap exhibits lower absorption and higher transmittance in the visible spectrum compared to the spincoated reference layer. This suggests that the bladecoated perovskite layer is still thinner than the spincoated one.

Another variable that directly influences the thickness of the blade-coated perovskite layer is the ink injection volume. The Figure 4a and Figure s4b present the influence of injected ink volume on optical properties of bladecoated perovskite films. As the injection volume increases, a larger volume of the ink accumulates in the meniscus at the front of the blade. Consequently, as the blade moves and spreads the ink across the substrate, a thicker layer is formed. The transmittance spectra of perovskite films printed with ink injection volumes of 2 μL and 3 μL were compared in Figure 4a while keeping other printing parameters constant (at a speed of 150 mm min^{-1} and a blade–substrate gap of 0.1 mm). With an increase in the ink injection volume to 3 μL, the transmittance in the visible region decreased compared to the 2 μL injection volume, likely due to the increased layer thickness. However, as observed in the optical images of the perovskite films inset in Figure 4a, which were consistently obtained for the 3 μL injection volume, a significant amount of ink is consumed at the beginning of the printing process. This leads to non-uniform perovskite layer thickness during printing. Based on these results, the optimal ink injection volume was determined to be 2 μL. The PL spectra in Figure 4b further reveal changes in radiative recombination behavior with thickness variation, indicating that optimized volume improves film uniformity and emission intensity. In addition, the effect of blade speed (100–400 mm min^{-1}) on device performance is systematically analyzed. Although the overall efficiencies remain relatively modest, a clear optimum is observed at 200 mm min^{-1}, where the device achieves the highest PCE of 9.24%, primarily due to a pronounced increase in shortcircuit current (J_{SC}) density (18.26 mA/cm^2). At lower speeds (100–150 mm min^{-1}), limited current density and moderate fill factor (FF) restrict performance, while excessively high speeds (≥300 mm min^{-1}) lead to reduced open-circuit voltage (V_{OC})and inconsistent current generation, likely due to nonuniform film formation and thickness fluctuations. These results demonstrate that careful control of ink volume and coating speed is critical for balancing film thickness, optical absorption, and charge transport to achieve optimal photovoltaic performance. The thickness of the perovskite absorber layer plays an important role in determining both optical absorption and charge collection efficiency. Increasing the film thickness generally enhances light absorption due to the high absorption coefficient of perovskite materials. However, excessively thick films may increase carrier recombination and limit efficient charge extraction. Conversely, thinner films can facilitate improved carrier collection but may reduce light harvesting if the absorber layer becomes too thin. Therefore, an optimal thickness is required to balance sufficient photon absorption with efficient charge transport and collection. Table 2. The summary table details the performance metrics, identifying 200 mm min^{-1} as the optimum blade speed, which yields the highest PCE of 9.24% due to a significant improvement in current density.

Figure 5 compares the photovoltaic performance and photoluminescence characteristics of perovskite solar cells fabricated by spin coating and blade coating using different precursor ink molarities. The statistical box plots summarize the variation in key device parameters, including PCE, J_{SC}, V_{OC}, and FF. Devices prepared by blade coating exhibit a generally higher V_{OC} compared with the spincoated counterparts, suggesting reduced nonradiative recombination and improved interfacial energetics. However, the bladecoated devices show lower J_{SC} and FF values, which ultimately limit the overall efficiency relative to spincoated devices. This reduction may be associated with differences in film thickness, crystallization dynamics, and charge transport properties induced by the bladecoating process and ink concentration. The J–V curves in Figure 5e further illustrate these trends, where the spincoated device demonstrates higher current density, while bladecoated films show reduced current output. In addition, the PL spectra reveal differences in emission intensity between the deposition methods and ink molarities, indicating variations in radiative recombination and film quality. Overall, the results highlight that while blade coating can enhance V_{OC}, further optimization of ink molarity and film formation is necessary to improve charge transport and increase J_{SC} and FF to achieve performance comparable to spincoated devices. Table 3 presents the photovoltaic parameters for cells with the highest efficiency. The maximum efficiencies of 9.24% and 11.84% were achieved for the perovskite layer blade-printed PSCs with the final optimized variables for perovskite inks with concentrations of 1 M and 1.5 M, respectively.

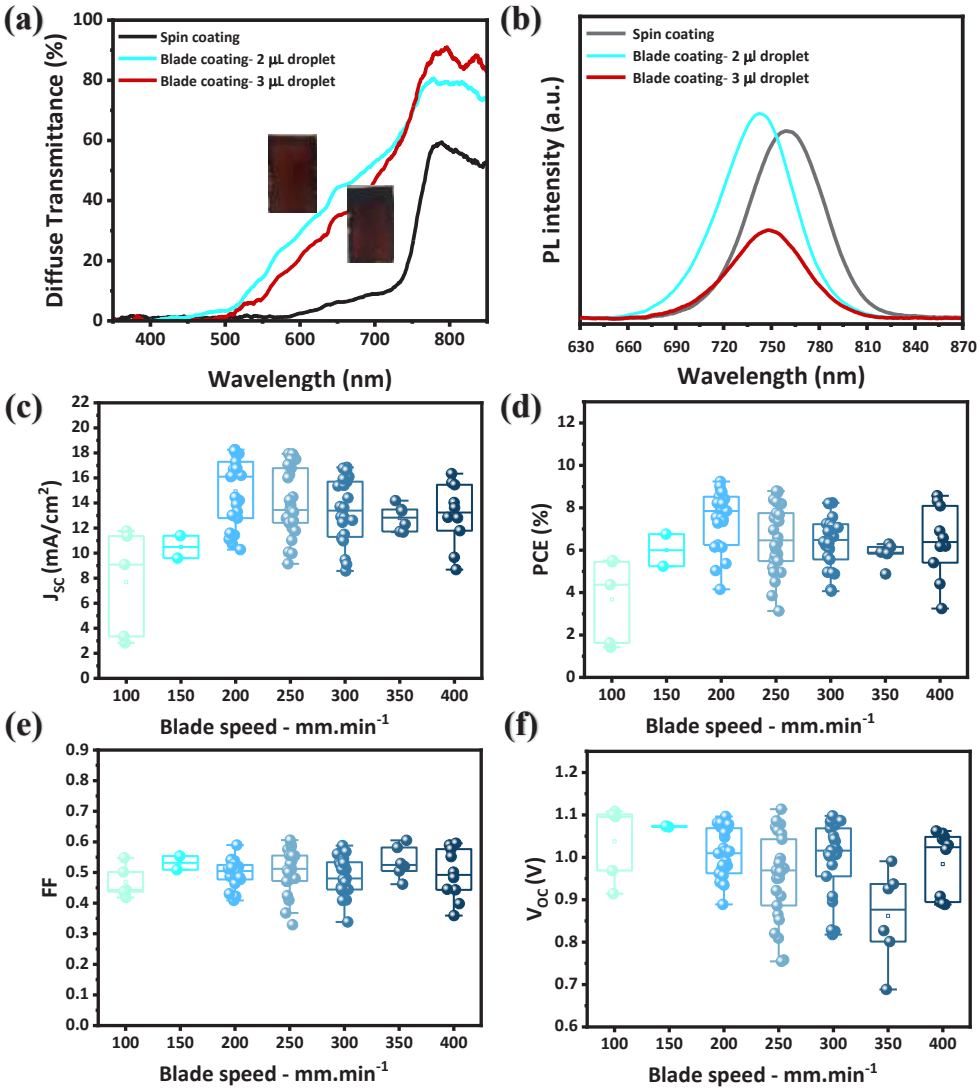

Fig. 4- (a) Optical transmittance spectra and (b) PL spectra of films prepared with different ink injection volumes (2 µL vs. 3 µL). (c-f) Statistical box plots illustrate the effect of blade speed (ranging from 100 to 400 mm min^{-1}) on the photovoltaic parameters.

Table 2- Performance parameters of blade coated perovskite solar cells fabricated at different coating speeds

Blade speed (mm min^{-1})	V_{OC} (V)	J_{SC} (mA/cm^2)	FF	PCE (%)
100	1.11	11.35	0.44	5.51
150	1.07	11.38	0.50	5.24
200	0.95	18.26	0.52	9.24
250	0.95	17.48	0.53	8.79
300	0.98	15.7	0.53	8.23
350	0.92	11.68	0.58	6.29
400	0.89	16.34	0.59	8.56

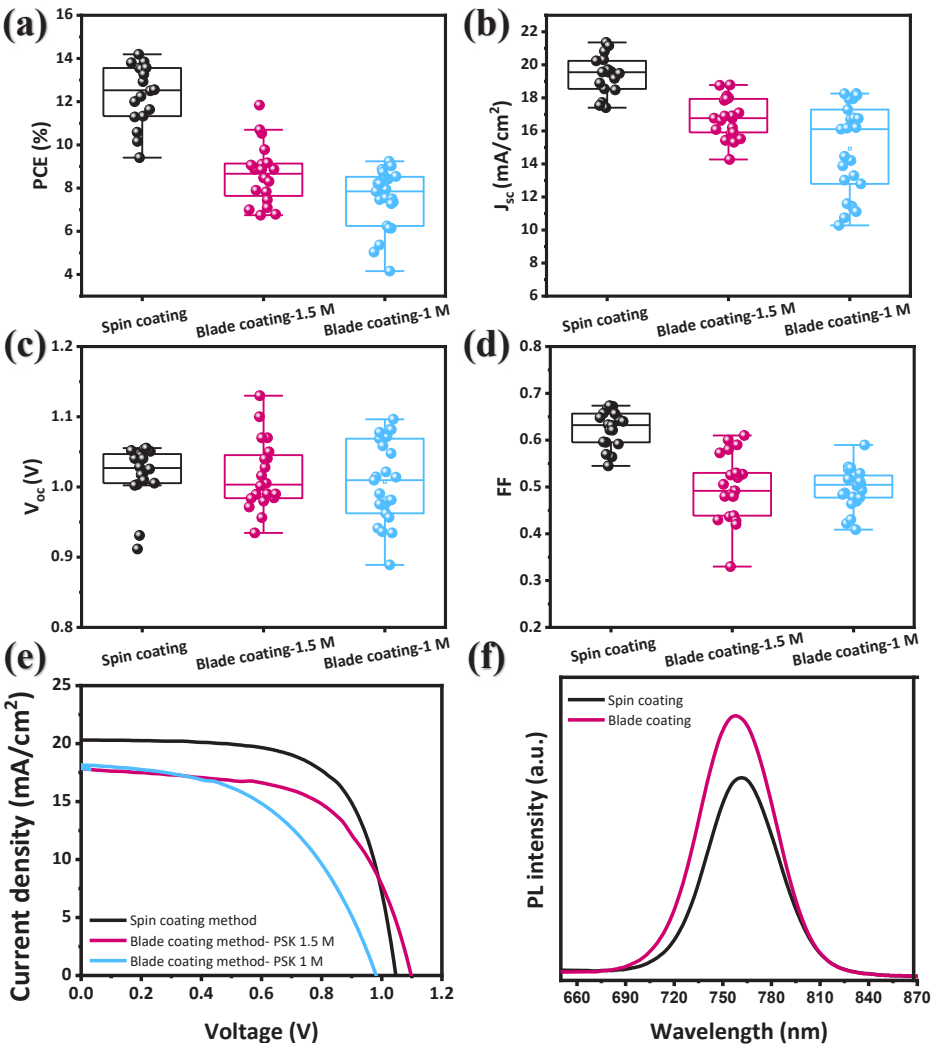

Fig. 5- Photovoltaic performance and optoelectronic characterization of perovskite solar cells comparing spin-coating and blade-coating methods with varying ink molarity. Statistical box plots for (a) PCE (b) J_{SC}, (c) V_{OC} and (d) FF, showing the impact of deposition technique and precursor concentration (1.5 M vs. 1 M). (e) J-V curves illustrating the superior V_{OC} but lower J_{SC} and FF for blade-coated devices compared to spin-coated ones. (f) PL spectra comparing the radiative recombination behavior of perovskite films prepared by both methods.

Table 3- Comparison of photovoltaic performance of perovskite solar cells fabricated via spin coating and blade coating under optimized processing conditions

Deposition method	Ink concentration (M)	Blade speed (mm min^{-1})	Gap (mm)	Ink injection (µL)	V_{OC} (V)	J_{SC} (mA/cm^2)	FF	PCE (%)
Spin coating	1.5	-	-	45	1.05	20.30	0.67	14.19
Blade coating	1.5	200	0.1	2	1.10	17.85	0.60	11.84
	1	200	0.1	2	0.95	18.26	0.52	9.24

Figure 6 compares the surface morphology of perovskite films deposited by spin coating and blade coating after optimization of the bladecoating parameters, examined at different FESEM magnifications. The spincoated film (a_1–a_3) shows a relatively non-uniform surface with the appearance of dark halo-like regions (indicated by arrows in a_3), suggesting compositional inhomogeneity or local variations in crystallization across the film. This occurs despite the fact that the spin coating process was carried out inside a dry box using the same precursor composition. The film also exhibits smaller grains and less well-defined grain boundaries at higher magnification.

In contrast, the bladecoated film (b_1–b_3), which was deposited under ambient conditions, displays a distinctly different morphology. The surface appears more uniform and is characterized by larger, more rounded grains with clearer grain boundaries. This difference in microstructure is attributed to the distinct crystallization dynamics during blade coating, where the controlled solvent evaporation and meniscus-guided film formation promote grain growth and improved structural organization. The comparison indicates that blade coating can produce a more homogeneous microstructure with larger grains even under ambient processing conditions.

One of the challenges in the blade-coating method at a large scale is the non-uniformity of layers during deposition, which can be due to the dynamics of the solution flow [3]. Additionally, the electron-transporting layer, typically used as the substrate for perovskite, often lacks suitable wettability, leading to reduced perovskite adhesion during blade coating. A technique used to create uniform layers involves incorporating a very small amount of surfactant (in the ppm range) into the perovskite ink [21,22]. Surfactants are compounds with a hydrophilic head and a hydrophobic tail. By adding them to the perovskite ink, the surface tension of the ink decreases, and with increased ink wettability on the substrate surface, it leads to the formation of uniform perovskite layers. In previous research by our group, in an n-i-p mesoporous structure using a mesoporous TiO_2 layer as the electron-transporting layer, a concentration of 12.5 mM TX-100 was added and optimized as a surfactant in the perovskite ink [23]. However, the optimization of TX-100 concentration for application in this planar n-i-p structure is needed to be investigated. Perovskite layers were fabricated on a Glass/SnO_2 substrate using the blade-coating method with perovskite ink containing various concentrations of TX-100.

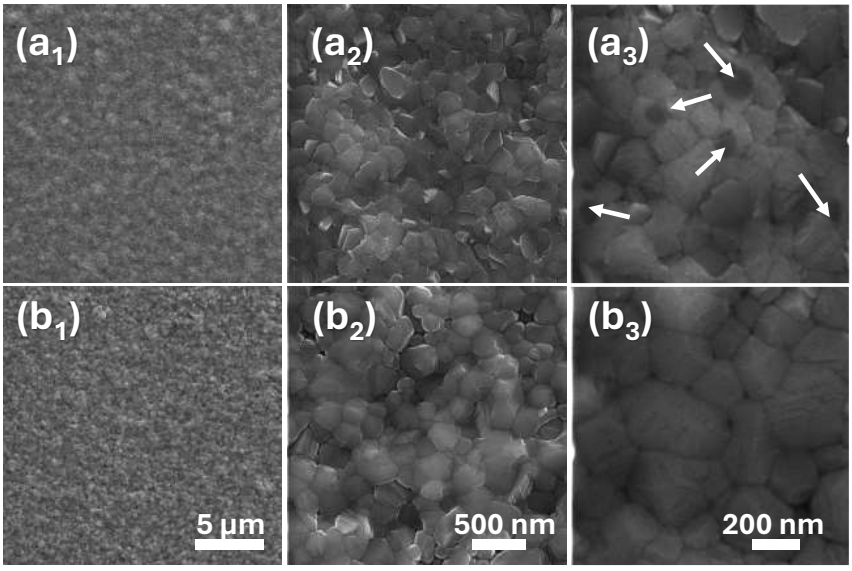

Fig. 6- Top-view FESEM images comparing the surface morphology of perovskite films deposited via (a_1–a_3) spin coating in a controlled dry box and (b_1–b_3) optimized blade coating in ambient conditions at different magnifications.

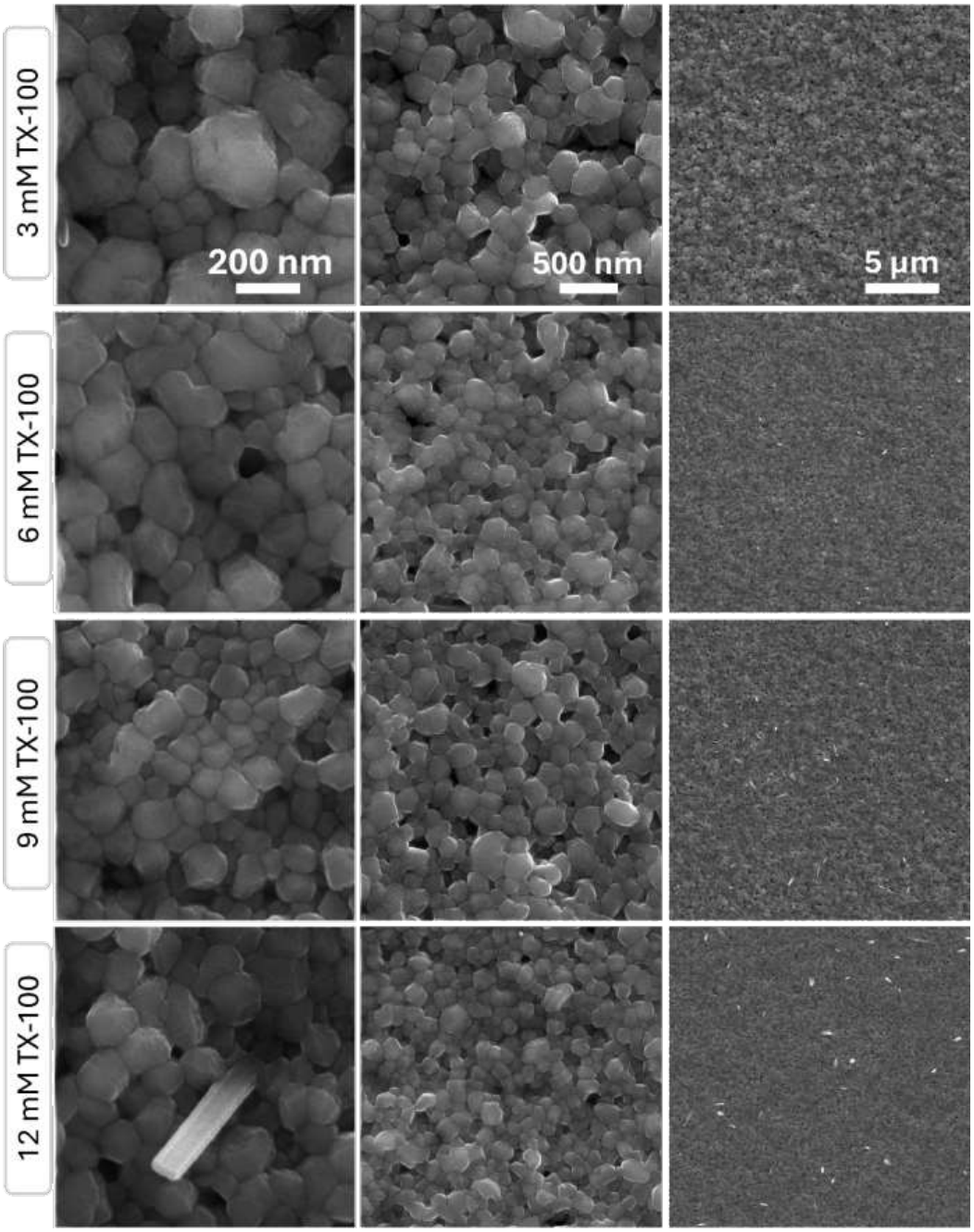

Fig. 7- FESEM images showing the effect of TX 100 concentration on the surface morphology of the films. Images in each row correspond to different magnifications with scale bars of 200 nm, 500 nm, and 5 µm (from left to right).

FESEM was employed to investigate the effect of TX100 surfactant on the surface morphology, grain size, and microstructure of the prepared films. The images were recorded in secondary electron (SE) mode using a MIRA3 TESCAN microscope at an accelerating voltage of 15 kV and a working distance of approximately 5 mm. As shown in the FESEM micrographs in Figure 7, the surface morphology was examined at different magnifications of 170 kX, 80 kX and 10 kX to analyze both the overall surface topography and largearea uniformity of the film and the grain-scale features. The FESEM images reveal a clear influence of TX100 concentration on the surface morphology and grain structure of the films. At a lower concentration of 3 mM TX100, relatively larger grains with well-defined boundaries are observed, indicating limited surface coverage by the surfactant and a crystal growth process dominated by grain coalescence. When the concentration increases to 6 mM, the microstructure becomes rougher and the average grain size slightly decreases, suggesting that TX100 begins to affect growth dynamics by interacting with the crystal surface and grain boundaries. At 9 mM TX100, a further reduction in grain size is observed, accompanied by a denser packing of grains. This behavior indicates that the higher surfactant concentration inhibits grain growth, leading to finer crystallites [10]. Finally, at 12 mM TX100, the grains become significantly smaller, and the surface appears smoother at the larger observation scale.

The optical and steady-state PL properties of the perovskite films were analyzed to understand the impact of TX-100 on charge carrier dynamics, as shown in Figure 8. The absorbance and transmittance spectra (Figure 8a-b) reveal that increasing the surfactant concentration from 3 mM to 12 mM leads to a progressive increase in transmittance and a decrease in absorbance. Despite the reduction in light absorption, the PL spectra (Figure 8c) demonstrate a dramatic enhancement in emission intensity as the TX-100 concentration increases. Usually, smaller grains—as observed in the FESEM analysis—would lead to a higher density of grain boundaries and increased non-radiative recombination [24,25]. However, the surfactant modification reverses this effect. As illustrated in the schematic in Figure 8d, the TX-100 molecules effectively passivate the grain boundaries. By "wrapping" around the smaller grains, the surfactant molecules neutralize trap states that would otherwise act as recombination centers.

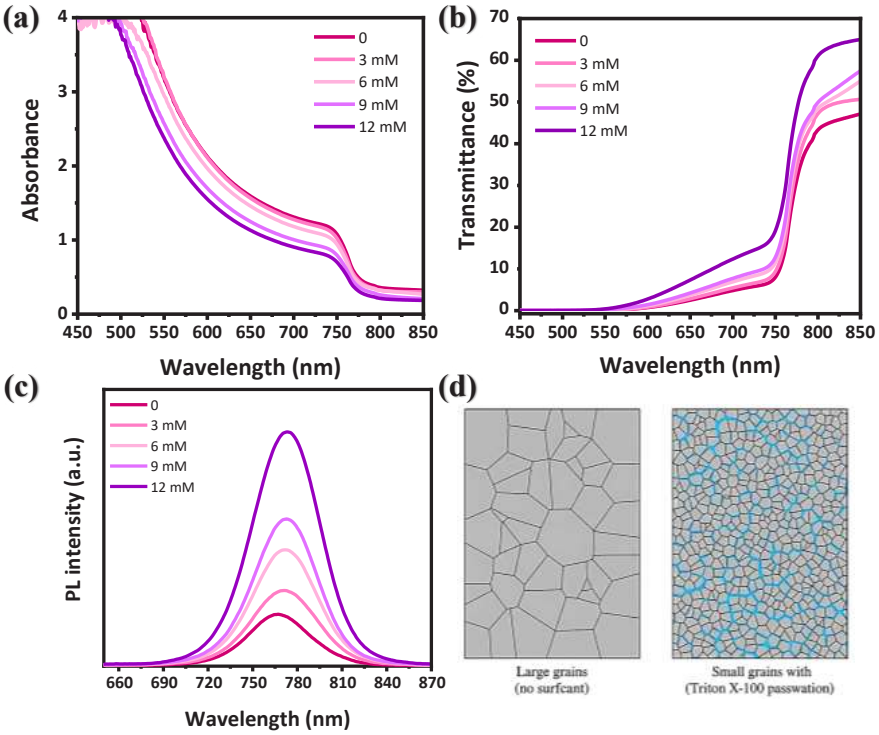

Fig. 8- Optical and photophysical characterization of perovskite films prepared with different TX 100 concentrations. (a) UV–Vis absorbance spectra and (b) UV–Vis transmittance spectra (c) PL spectra showing enhanced emission intensity with increasing TX 100 concentration, indicating reduced non radiative recombination due to defect passivation. (d) Schematic illustration of the proposed mechanism, where TX 100 molecules passivate grain boundaries, leading to modified grain growth and improved optoelectronic properties compared with films prepared without surfactant.

As shown in FESEM top surface in Figure 7, by increasing the concentrations of TX-100, the surface morphology undergoes a distinct change characterized by the emergence of long rod-shaped structures embedded within the primary perovskite matrix. Based on the elemental map analysis in Figure 9 (a), they do not show any composition change relative to the matrix. Furthermore, the cross-sectional SEM images in Figure 9(b) were utilized to investigate the variation in film thickness. By applying the relationship shown in Equation 1, which correlates the absorption coefficient (α) with the transmittance (T) and thickness (d) at a specific wavelength (λ=555 nm), it was determined that the total film thickness decreases as the TX-100 concentration increases. This reduction in thickness, supported by the absorbance data, indicates that the surfactant influences the rheological properties of the ink.

The combination of stronger PL emission and thinner perovskite layers is particularly relevant for lightemitting applications, as efficient radiative recombination and controlled film thickness are key requirements for perovskite-based lightemitting diodes (PeLEDs). Therefore, these observations suggest that TX100–assisted blade coating may provide a promising pathway for engineering perovskite films suitable not only for photovoltaic devices but also for future development of printed perovskite-based LEDs [26,27].

The photovoltaic performance of the perovskite solar cells was systematically evaluated as a function of TX100 concentration from 0 to 12 mM, as summarized in Figure 10 and Table 4. The data reveals a clear dependence of device performance on the amount of surfactant incorporated into the perovskite ink. At low concentrations (2–6 mM), the surfactant improves several key photovoltaic parameters, whereas higher concentrations lead to pronounced performance degradation. Among the tested formulations, the device containing 2 mM TX100 delivers the best overall results, achieving a maximum PCE of 14.76%, with a high J_{SC} of 20.69 mA cm^{-2} and an average PCE of 13.83%. The 4 mM and 6 mM devices also exhibit competitive champion efficiencies of 14.26% and 14.48%, respectively, although their average PCE values show a slight decline. Notably, the 4 mM device displays the highest fill factor (FF = 0.73, Max), suggesting enhanced charge extraction and reduced interfacial recombination at this concentration. The V_{OC} gradually increases with TX100 concentration, rising from 1.05 V (0 mM) to 1.08 V (8 mM). Even at the highest concentrations

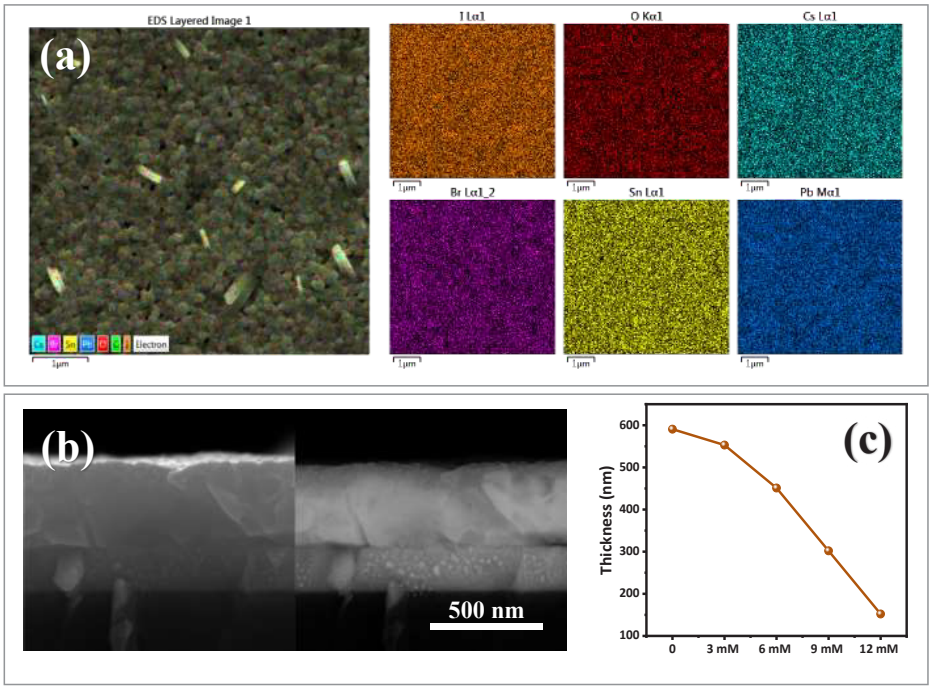

Fig. 9- Elemental mapping and structural analysis of the perovskite films. (a) Top-view FESEM image with corresponding EDS elemental maps for Cs, Br, Sn, Pb, O, and C, showing the uniform distribution of elements across the film surface; the presence of rod-like structures is visible at high TX-100 concentrations. (b) Cross-sectional FESEM images of the device stack and a graph illustrating the decreasing trend in perovskite film thickness as a function of increasing TX-100 concentration, consistent with the absorbance data and the Beer-Lambert relationship.

(10–12 mM), V_{OC} remains relatively high (1.05–1.06 V). This improvement is consistent with the expected passivation effect of TX100, which reduces nonradiative recombination and increases quasiFermi level splitting.

Despite this, both J_{SC} and FF decrease significantly at high surfactant concentrations. For instance, the champion J_{SC} drops from 20.69 mA cm^{-2} at 2 mM to 16.21 mA cm^{-2} at 10 mM and further to 10.26 mA cm^{-2} at 12 mM. The FF similarly declines from 0.68–0.73 (2–4 mM) to just 0.42 and 0.41 at 10 mM and 12 mM, respectively. As a result, the maximum PCE decreases sharply to 7.21% at 10 mM and 4.45% at 12 mM, with average efficiencies falling even more dramatically.

The simultaneous reduction in J_{SC} and FF at elevated TX100 concentrations is attributed to two key factors: (1) Reduced perovskite film thickness, consistent with the lower absorption observed in the optical spectra at high surfactant loadings. (2) Accumulation of insulating surfactant molecules at grain boundaries, which can hinder charge carrier mobility and increase series resistance. Overall, low TX100 concentrations (particularly 2–4 mM) promote more balanced photovoltaic behavior, combining enhanced V_{OC}, high J_{SC}, and robust FF. In contrast, excessively high concentrations (>8 mM) disrupt charge transport and severely limit light harvesting, despite retaining relatively high V_{OC}. Table 4 highlights this tradeoff clearly, illustrating that 2 mM TX100 offers the optimal balance of voltage enhancement, current generation, and fillfactor stability, making it the most effective concentration for performance improvement.

The trends observed in the J–V measurements are further supported by the IPCE spectra of the devices in Figure 10f. The IPCE intensity decreases progressively as the TX100 concentration increases, consistent with the reduction in J_{SC} extracted from the J–V curves. At low surfactant loadings (2–6 mM), the devices maintain relatively high IPCE values across the visible spectrum, confirming efficient photontoelectron conversion and strong optical absorption. However, at higher concentrations (≥8 mM), the IPCE response drops sharply, particularly in the 450–750 nm region, indicating reduced light harvesting and poorer charge collection. This reduction aligns with the thinner perovskite films and the increased interfacial resistance induced by excess surfactant molecules. For the poorly performing devices (10–12 mM TX100), a more pronounced discrepancy is observed between the J_{SC} obtained from the J–V curves and that calculated by integrating the IPCE spectra. This mismatch can be attributed to device heating during measurement under the solar simulator. Under constant illumination, the weak devices experience significant seriesresistanceinduced heating, which artificially depresses the J_{SC} during the J–V scan, while the IPCE measurement—performed under LED and much lowerpower illumination—does not induce such thermal stress. As a result, the J–Vderived J_{SC} values are underestimated relative to the IPCEintegrated currents. This effect becomes particularly prominent in the 10 and 12 mM devices, where excessive TX100 severely hinders charge transport and increases resistive losses.

Table 4- Summary of photovoltaic parameters of perovskite solar cells fabricated using inks containing different concentrations of TX 100

TX-100 concentration (mM)		V_{OC} (V)	J_{SC} (mA/cm^2)	PCE (%)	FF
0	Max	1.05	19.65	13.55	0.66
	Avg	1.07	19.28	12.00	0.59
2	Max	1.06	20.69	14.76	0.68
	Avg	1.07	19.69	13.83	0.66
4	Max	1.06	18.50	14.26	0.73
	Avg	1.06	19.38	12.77	0.63
6	Max	1.07	19.67	14.48	0.69
	Avg	1.06	19.45	11.96	0.58
8	Max	1.08	18.89	13.55	0.67
	Avg	1.07	17.76	9.68	0.51
10	Max	1.05	16.21	7.21	0.42
	Avg	1.04	13.70	5.55	0.39
12	Max	1.06	10.26	4.45	0.41
	Avg	1.00	7.58	2.49	0.32

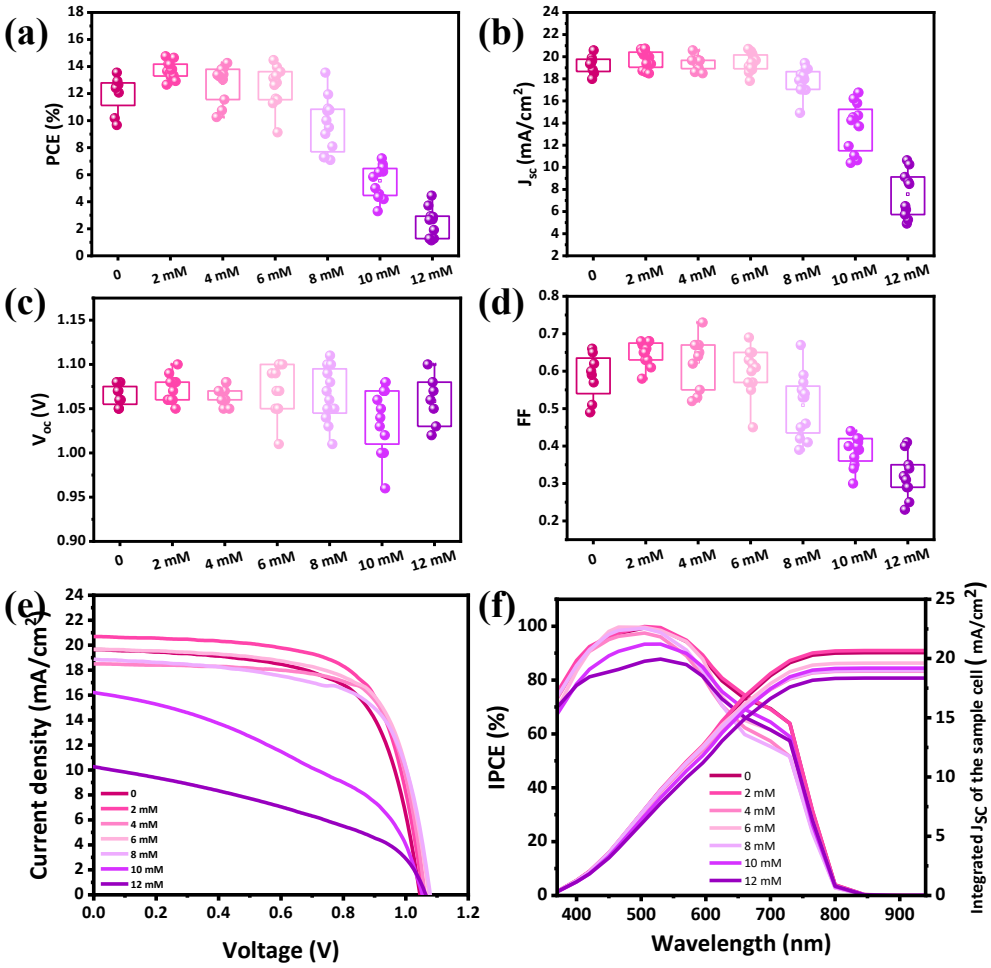

Fig. 10- Photovoltaic performance statistics and optoelectronic characterization of perovskite solar cells fabricated with different TX-100 concentrations. Box plots showing the distribution of (a) PCE, (b) J_{SC}, (c) V_{OC}, and (d) FF for the fabricated devices. (e) The champion J-V curve and (f) IPCE of the corresponding devices.

4. Conclusion

In this study, PSCs were systematically optimized under ambient conditions, with particular attention to the role of the nonionic surfactant TX-100 as a morphology and performance modifier. Careful tuning of blade-coating parameters established a robust baseline and enabled a direct evaluation of TX-100 across a range of concentrations from 0 to 12 mM. Quantitative device analysis revealed a strong dependence on TX-100 concentration: Cells fabricated without TX-100 (0 mM) displayed a PCE of 13.55% (average 12.00%). Incorporating TX-100 at 2 mM yielded the optimum performance, with a champion PCE of 14.76% and an average PCE of 13.83%, reflecting enhancements in short-circuit current density, fill factor, and overall film quality. Devices with 4 mM and 6 mM TX-100 also showed relatively high efficiencies (typical champion PCEs above 13%), but further increases in surfactant loading led to pronounced performance declines.

At 8 mM TX-100, device PCE decreased sharply, and cells with 10 mM and 12 mM exhibited severe efficiency losses (PCEs of 7.21% and 4.45%, respectively). This degradation was attributed to excessively thin films, decreased grain size, and impaired charge transport, as confirmed by morphological, optical, and photoluminescence analyses. High TX-100 concentrations also increased discrepancies between J-V and IPCE-derived photocurrents—a sign of non-ideal charge extraction and measurement artifacts.

References

1. Green, M. A. et al. Resource Solar cell efficiency tables : Version 68 Solar cell efficiency tables : Version 68. Joule 102494 (2026) doi:10.1016/j.joule.2026.102494.
2. Kim, H.-S. & Park, N.-G. Design of perovskite ink for scalable solution process. Appl. Phys. Rev. 12, (2025).
3. Hu, H. et al. Nucleation and crystal growth control for scalable solution-processed organic–inorganic hybrid perovskite solar cells. J. Mater. Chem. A 8, 1578–1603 (2020).
4. Wan, Z. et al. Scalable fabrication of high-efficiency FAPbI3 perovskite solar modules in humid air via intermediate-phase engineering. Joule (2026).
5. Chu, L., Cao, J. & Wu, C. Methylammonium-Free Perovskite Photovoltaic Modules. ACS Nano 19, 13527–13548 (2025).
6. Jiang, Y. Scalable Fabrication of High Efficiency Hybrid Perovskite Solar Cells by Electrospray. (2019).
7. Mateen, M. et al. High-performance mixed-cation mixed-halide perovskite solar cells enabled by a facile intermediate engineering technique. J. Power Sources 448, 227386 (2020).
8. Adhyaksa, G. W. P. et al. Carrier diffusion lengths in hybrid perovskites: processing, composition, aging, and surface passivation effects. Chem. Mater. 28, 5259–5263 (2016).
9. Maschwitz, T. et al. How crystallization additives govern halide perovskite grain growth. Nat. Commun. 16, 9894 (2025).
10. Wang, W. et al. The growth dynamics of organic–inorganic metal halide perovskite films. J. Am. Chem. Soc. 144, 17848–17856 (2022).
11. Li, J. Rational ink design and combinatorial slot-die coating of metal halide perovskites for solar cells. (2023).
12. Wu, Z., Li, W., Ye, Y., Li, X. & Lin, H. Recent progress in meniscus coating for large-area perovskite solar cells and solar modules. Sustain. Energy Fuels 5, 1926–1951 (2021).
13. Dunlap-Shohl, W. A., Zhou, Y., Padture, N. P. & Mitzi, D. B. Synthetic approaches for halide perovskite thin films. Chem. Rev. 119, 3193–3295 (2018).
14. Liu, Y. et al. Stabilized perovskite ink for scalable coating enables high-efficiency perovskite modules. Sci. Adv. 12, eaec0915 (2026).
15. Heidariramsheh, M., Jalalichamani, H., Shabanzadeh, M., Mahdavi, S. M. & Taghavinia, N. Comparison of meniscus-printed Cu2Sn (S, Se) 3 and Cu2ZnxSn (S, Se) 4 thin films to apply in superstrate solar cells. Mater. Res. Bull. 184, 113243 (2025).
16. Deng, Y. et al. high-speed deposition of perovskite films for efficient photovoltaic modules. Nat. Energy 3, (2018).
17. Sha, N. et al. Surface passivation by CTAB toward highly efficient and stable perovskite solar cells. Appl. Surf. Sci. 635, 157643 (2023).
18. Huang, X. et al. Polyanionic surfactant modulates the substrate surface energy to achieve crystallization control for efficient perovskite solar cells. J. Mater. Chem. A 13, 36987–36996 (2025).
19. Dai, X., Deng, Y., Van Brackle, C. H. & Huang, J. Meniscus fabrication of halide perovskite thin films at high throughput for large area and low-cost solar panels. Int. J. Extrem. Manuf. 1, 22004 (2019).
20. Solé, J., Bausa, L. & Jaque, D. An introduction to the optical spectroscopy of inorganic solids. (John Wiley & Sons, 2005).
21. Wang, L. et al. Surfactant engineering for perovskite solar cells and submodules. Matter 6, 2987–3005 (2023).
22. Yang, X. et al. Blade-coating perovskites for tandem devices: liquid mechanism, film formation, and performance. Sol. RRL 9, 2500149 (2025).
23. Parvazian, E., Abdollah-Zadeh, A., Dehghani, M. & Taghavinia, N. Photovoltaic Performance Improvement in Vacuum-Assisted Meniscus Printed Triple-Cation Mixed-Halide Perovskite Films by Surfactant Engineering. ACS Appl. Energy Mater. 2, 6209–6217 (2019).
24. Zhou, Y., Herz, L. M., Jen, A. K. Y. & Saliba, M. Nat. Energy 7, 794–807 (2022).
25. Ahmad, S. et al. Sequential organic ligand modifications to dedicatedly restructure grain boundary and surface of perovskites. Nat. Commun. (2025).
26. Lin, K. et al. Perovskite light-emitting diodes with external quantum efficiency exceeding 20 per cent. Nature 562, 245–248 (2018).
27. Tan, Z.-K. et al. Bright light-emitting diodes based on organometal halide perovskite. Nat. Nanotechnol. 9, 687–692 (2014).